Summary of the 3rd GISMO pool

I. Hermelo, C. Kramer, M. González, and N. Billot

July 18, 2013

Abstract

The 3rd Goddard-IRAM Superconducting 2 mm Observer camera (GISMO) pool took place from April 9th to April 30th, 2013. During the two first weeks of the pool the weather conditions were favorable, allowing to observe a total of 130 hours. During the third week, bad weather heavily hindered the pool, allowing observations only for a total of 25 hours. Data for 18 of 22 projects were collected, and for three of them the total amount of allocated hours was reached.

Two standard observing modes were offered to perform the observations: the on-the-fly mode and the Lissajous mode. For the on-the-fly mode, appropriate for large maps, data are taken while the telescope follows a traditional zig-zag pattern, whereas for the Lissajous mode data are taken while the telescope follows a Lissajous curve pattern.

The median value of the opacities measured with the new taumeter was $\tau_{225\mathrm{GHz}} = 0.32 \pm 0.13$. The 48% of the ∼2400 scan collected were taken for projects of the good weather queue (e.g., deep fields, star forming regions with faint extended structures, low-mass prestellar cores), 17% for projects of the bad weather queue (e.g., lensed galaxies, active galactic nucleus, supernova remnants), and the remaining 35% were taken under the "test" project, which was used when unstable weather conditions or technical problems did not allow to observe properly. Besides, during the pool skydips with GISMO were carried out in order to check the values obtained with the taumeter. Both measurements show a positive correlation although the dispersion is high.

GISMO behavior during the 3rd pool was excellent in terms of stability with the exception of a leak in the GISMO cryostat that was identified on Sunday, April 7, during the cooling down of the system, and the overload of the GISMO server in the receiver cabin on Wednesday, April 17, which produced occasional corrupt packets. The helium recycling was done once a day from 7:00 to 9:30 (UT), whereas the refilling of the nitrogen was done twice a day, the first one during the helium recycling and the second from 18:00 to 18:30 (UT).

The median value of healthy pixels was 96 and the median value of the noise equivalent flux density was 14.6 mJy $\sqrt{\mathrm{s}}$. As previously noticed during the 1st and the 2nd GISMO pools, the number of healthy channels and the noise equivalent flux density show a dependence on the scan speed.

Uranus was used as primary calibrator. A total of 14 healthy scans were considered to study the flux stability. These scans were reduced manually using the last stable version of crush (v 2.14-2)

and the filtering scheme for point sources. The median value of the peak flux density per beam was 14.00 Jy, with an rms of 1.06 Jy (7.5%), in good agreement with the expected value.

1 Pool statistics

A total of 408 hours were scheduled at the IRAM 30m radiotelescope for the 3rd GISMO pool from April 9th to April 30th, 2013. Despite the good weather conditions, specially during the two first weeks, and the absence of technical problems, only 38% of the total amount of hours allocated were observed. For three projects (198-12, D12-12, D13-12) the total amount of allocated time was reached. On the other hand, the bad weather during the last week of the pool did not allow to observe most of the projects scheduled for this week.

We want to note that the analysis of the observed time described above it is based on the GISMO Nexus logsheet and therefore, it only includes the integration time on targets and pointing sources. In order to estimate the slewing time used to move the antenna between targets and pointing sources, $t_{\rm slew}$, we search in the GISMO Nexus logsheet for pointing scans preceded and followed by target scans. If $t_{\rm n}^{\rm point}$ is the time spent on the nth pointing scan, and $t_{\rm n-1}^{\rm fin}$ and $t_{\rm n+1}^{\rm ini}$ are the final and the initial time of the previous and the following target scans, respectively, then $t_{\rm slew}$ can be estimated as:

$$t_{\rm slew} = t_{\rm n-1}^{\rm fin} - t_{\rm n+1}^{\rm ini} - t_{\rm n}^{\rm point} \quad (1)$$

We found 90 occurrences of the sequence **target** $\rightarrow$ **pointing** $\rightarrow$ **target**. The median value of $t_{\rm slew}$ was 5.6 minutes. If we take into account $t_{\rm slew}$, the percentage of total time observed increases to 44% of the allocated time. The overheads, including the slewing time, range from $\sim$15% in the case of single field projects , to $\sim$30% for projects with a large number of targets spread over the sky .

2 Atmospheric opacity

Slewed skydips were done during the three weeks of the pool in order to calibrate GISMO and test the reliability of the new taumeter. For the skydip scans the automatically relock of the detectors before each scan was deactivated. Some of the curves showed a flattening of the signal above 50 degrees and below 25 degrees of elevation. For this reason we constrained the elevation to the range from 25 to 50 degrees to fit the opacity (see Figure 1).

The value of the opacity measured with the taumeter was obtained averaging the values of the opacities registered before and after the skydip scan. The skydips were reduced using the last stable version of crush (v 2.13-1). To scale the value obtained with the skydips (τ_{150GHz}) to the opacity measured with the taumeter (τ_{225GHz}) we adopted the ratio $\tau_{225GHz}/\tau_{150GHz}$=2.5 derived from the atmospheric model ATM (Pardo et al. 2001). A positive correlation was obtained between both measurements, although with a high dispersion (see Figure 2).

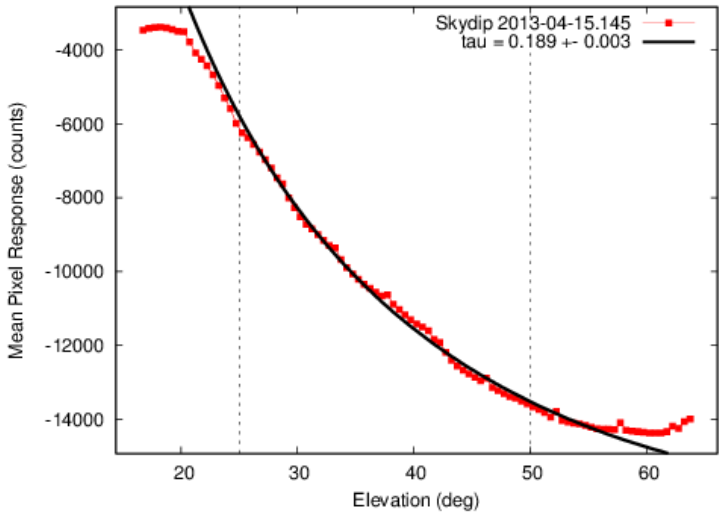

Figure 1: Skydips reduction obtained with crush.

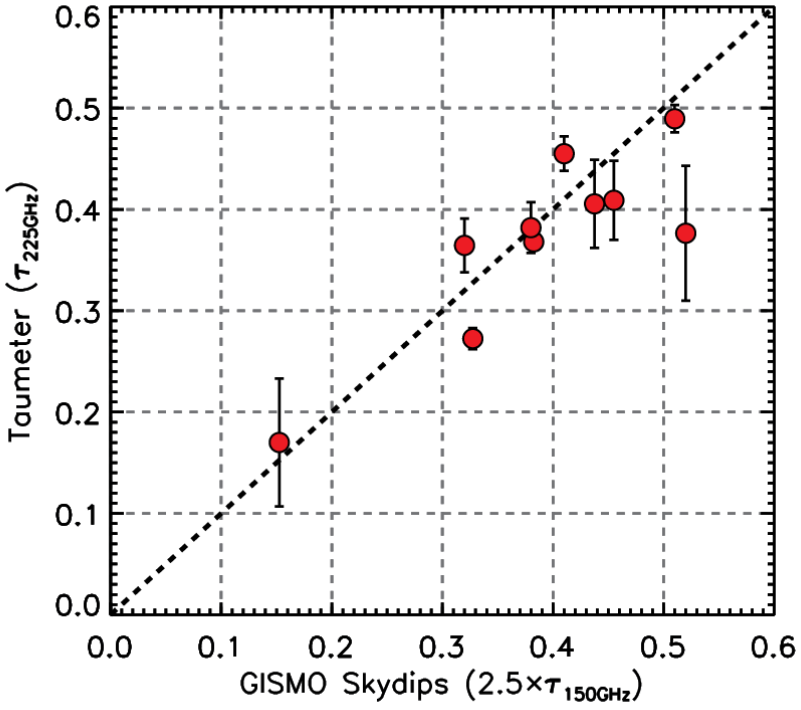

Figure 2: Comparison of the opacity measured by the taumeter and the opacity measured with skydips. The black dashed corresponds to the line 1:1.

3 Sensitivity

A total of 1076 target scans were considered for the sensitivity estimation (pointing and focus scans, as well as target scans taken under the "test" project, were rejected). The median value of the noise equivalent flux density for these scans is 14.6 mJy $\sqrt{\text{s}}$. We want to note that this value, obtained directly from the GISMO Nexus logsheet, corresponds to the noise equivalent flux density of the instrument projected out of atmosphere. The total noise equivalent flux density, hereafter NEFD$'$, which is the combined instrument and atmospheric noise equivalent flux density, can be calculated as:

$$\text{NEFD}' = \text{NEFD}\ \text{e}^{\tau_{150\text{GHz}}/\sin(\text{Elevation})} \tag{2}$$

As previously noticed during the 2nd pool (see Bruni & Kramer 2012), the noise equivalent flux density seems to improve at velocities above $60\,''/s$. During the 3rd GISMO pool a total of 690 target scans with scan velocities above $60\,''/s$ were collected. If we only consider these scans, the median value of the NEFD is 12.6 mJy $\sqrt{\text{s}}$. On the other hand, if only the scans with velocities under $60\,''/s$ are considered, the median value of the NEFD increases to 17.9 mJy $\sqrt{\text{s}}$. The trend with the scan speed is clearly visible in Table 1 and in Figure 3.

Project number	$< 60\,arcsec\,s^{-1}$				$> 60\,arcsec\,s^{-1}$			
	N	s	τ	NEFD	N	s	τ	NEFD
157-12	16	43.70	0.285	31.19				
170-12	1	34.50	0.331	23.39	10	76.10	0.304	17.89
196-12	11	44.10	0.337	30.90	36	76.00	0.422	12.00
198-12	45	43.90	0.265	18.60				
222-12	66	43.90	0.471	17.70				
223-12	25	45.70	0.373	21.60				
226-12					58	68.50	0.279	13.90
227-12	18	37.40	0.279	17.20	223	132.3	0.288	11.20
D12-12	10	43.90	0.120	15.79				
D13-12					175	76.00	0.242	13.10
D11-12	9	43.80	0.622	17.30				
221-12	47	43.90	0.327	17.20				
D07-12					96	66.10	0.284	11.80
195-12	45	44.10	0.468	17.80				
197-12	33	48.70	0.386	16.60	49	76.00	0.284	12.90
209-12	19	38.10	0.633	15.69				
225-12	21	43.80	0.407	19.20				
171-12	5	45.60	0.453	29.20				
213-12	15	45.70	0.363	18.50	43	76.00	0.279	13.60

Table 1: Values of the NEFD reached for each project. When possible, the analysis was separated between scan velocities below (middle panel) and above (right panel) $60\,''/s$. The four columns in these two panels correspond to the number of scans (N), the median scan speed (s), the median opacity (τ), and the median NEFD.

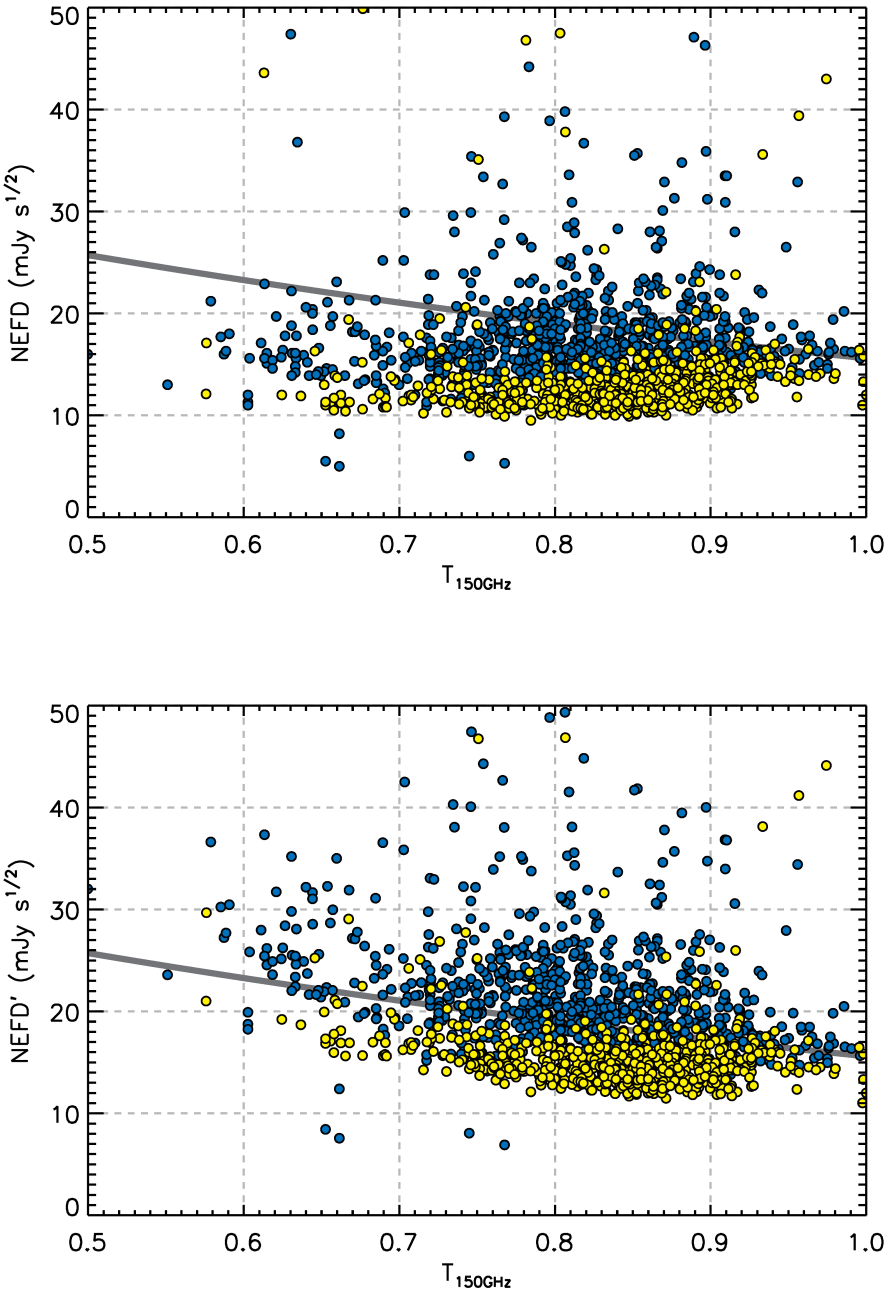

Figure 3: NEFD (top) and NEFD′ (bottom) *vs* transmission at 150 GHz for the cases of a scan speed under (blue) and over (yellow) $60\,''/s$. The gray line showing the expected trend of NEFD′ (see Equation 2) has been included for reference.

4 Pointing, focus and calibration

Although pointing constants are not really needed in the case of filled arrays, pointing corrections were systematically done every 60-90 minutes during the 3rd GISMO pool. The pointing scans consisted on $1.5' \times 1.5'$ Lissajous maps. The median value and the rms for the pointing corrections in azimuth and elevation are $\Delta\mathrm{Az} = -0.5 \pm 7.9$ and $\Delta\mathrm{El} = 0.6 \pm 6.9$, respectively. The pointing corrections for GISMO are larger than the typical values obtained with the heterodyne receivers. This is due to the fact that the automatic pointing corrections implemented in the system are optimized for the heterodyne receivers. Nevertheless, pointing sources were always detected within the array, and in 90% of the cases the peak is located within the central pixel (see Figure 4).

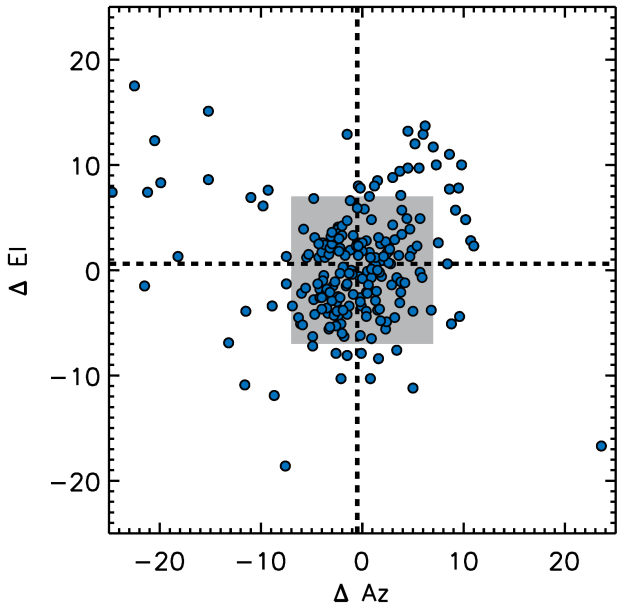

Figure 4: Pointing corrections applied during the GISMO pool. The gray shaded area represents the GISMO pixel size. The black dashed lines correspond to the median values found for ΔAz and ΔEl.

Focus corrections were based on five consecutive $1.5' \times 1.5'$ Lissajous maps taken at five different focus values ($\Delta\mathrm{Z_{current}}$, $\Delta\mathrm{Z_{current}} \pm 0.6\,\mathrm{mm}$, $\Delta\mathrm{Z_{current}} \pm 1.2\,\mathrm{mm}$). Focus corrections were calculated with second order fits to the integrated intensity and the FWHM (see Figure 5). The new value of the focus was determined as the value that maximizes the flux and minimizes the FWHM. The day time evolution of focus corrections were well behaved and predictable. The median value and the rms of the values used is $\Delta\mathrm{Z} = -1.8 \pm 0.7\,\mathrm{mm}$ (see Figure 6).

The Jy/counts factor of 30.5 used to calibrate the data was obtained during the 1st GISMO pool (Bruni et al. 2012) assuming a flux for Neptune of 6.27 Jy (`astro/gildas`). Only 10 healthy scans[1] of Neptune were collected during the 3rd pool (see Table 2 and Figure 7), with a median value of 5.93 Jy and a rms of 0.64 Jy (10.8%), in good agreement with the value from `astro/gildas`.

[1] I.e., those scans with more than 90 healthy channels, FWHM lower than $21''$, elevation higher than 25 degrees, and $\tau_{225\,\mathrm{GHz}}$ below 0.4.

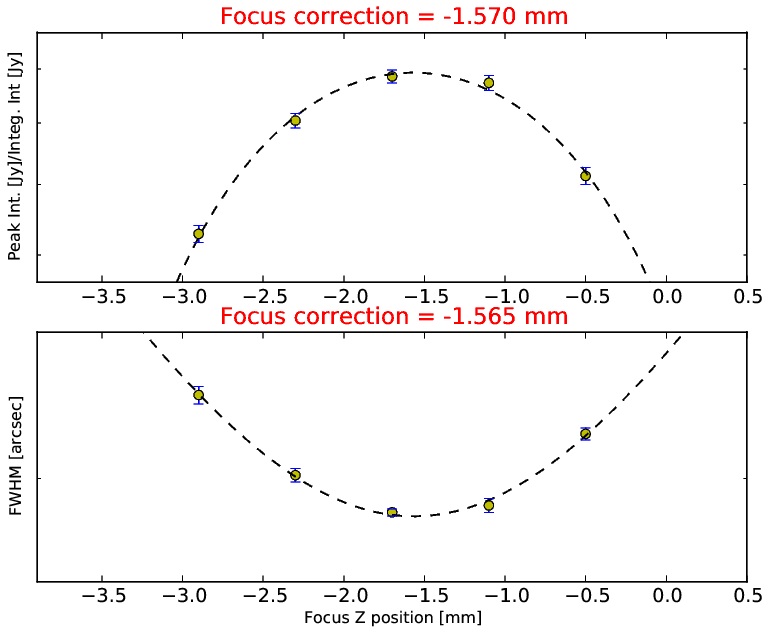

Figure 5: Example of the second order fit to the integrated intensity (top) and to the FWHM (bottom) used to calculate the focus corrections.

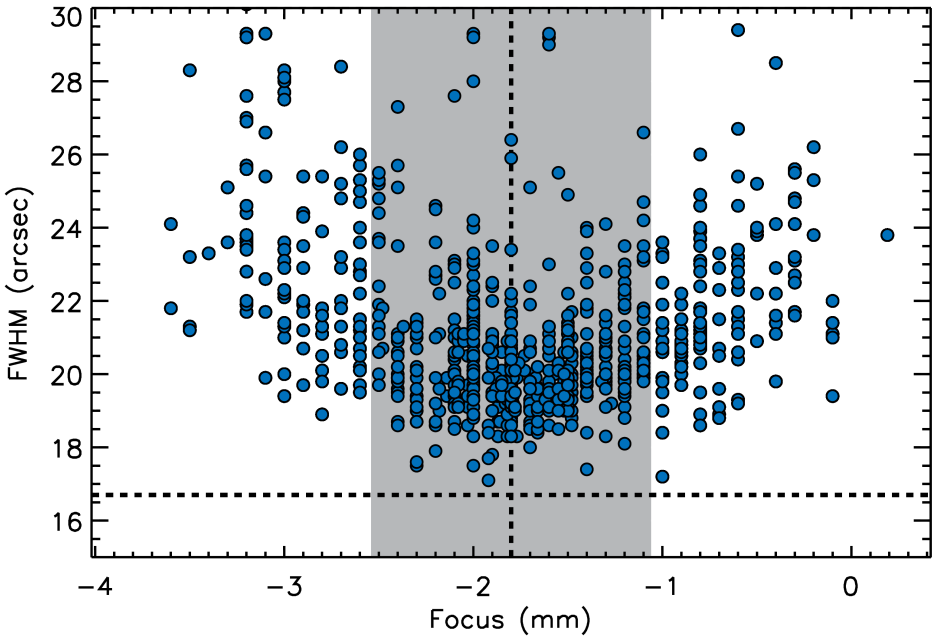

Figure 6: Focus corrections used during the GISMO pool. The vertical black dashed line and the gray shaded area correspond to the median value and to the rms, respectively. The horizontal black dashed line corresponds to the half-power beamwidth of the telescope (16.7″).

For Uranus, which was used as primary calibrator of the 3rd GISMO pool, a total of 14 healthy scans were taken with a median flux of 14.00 Jy and a rms of 1.06 Jy (7.5%). In this case the expected value of the flux is 15.0 Jy (`astro/gildas`), thus confirming the Jy/counts factor. Using Bolocam data collected between 2003 and 2010, Sayers et al. (2012) derived for Uranus a 143 GHz brightness temperature of 106.6 ± 3.5 K. From the flux measured with GISMO, scaled using the ratio $F_{143GHz}/F_{150GHz} = 0.927$ (`astro/gildas`), we obtained 106.1 K, in perfect agreement with the value reported by Sayers et al. (2012).

Calibrator	Number of scans	Flux Jy	ΔFlux Jy	ΔFlux %	FWHM arcsec
Neptune	10	5.93	0.64	10.8	19.4
Uranus	14	14.00	1.06	7.5	20.6

Table 2: Peak flux density per beam of the primary calibrators Neptune and Uranus based on the data collected during the 3rd GISMO pool.

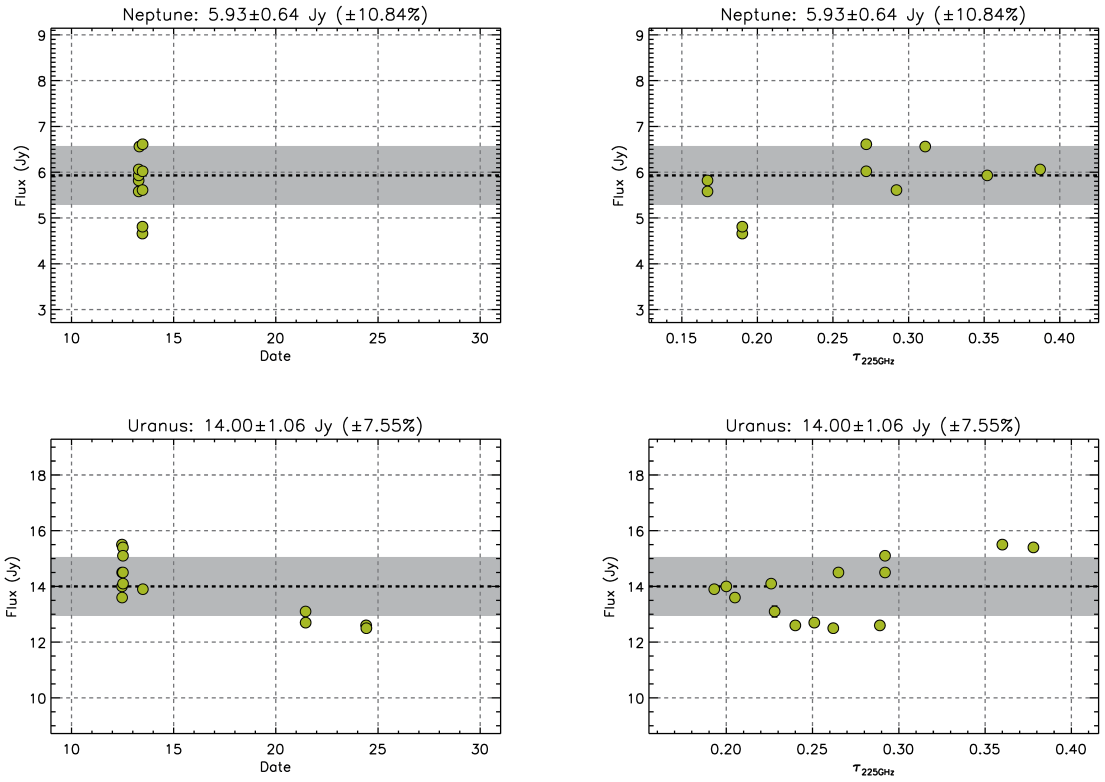

Figure 7: Peak flux density per beam of Neptune (top) and Uranus (bottom) *vs* date (left) and $\tau_{225\,GHz}$ (right). The black dashed and the gray shaded area correspond to the median value and to the rms, respectively.

5 Beam map

Several beam map scans, designed to ensure the source is moved over the entire detector, were carried out in order to check the pixel position in the field of view as well as the source and sky gains. Instead of making a single map from all pixels, crush creates separate maps for each pixel and calculates the actual pixel offsets in the focal plane. Figure 8 shows the pixel position and the sky gain for one of the beam maps collected during the 3rd pool.

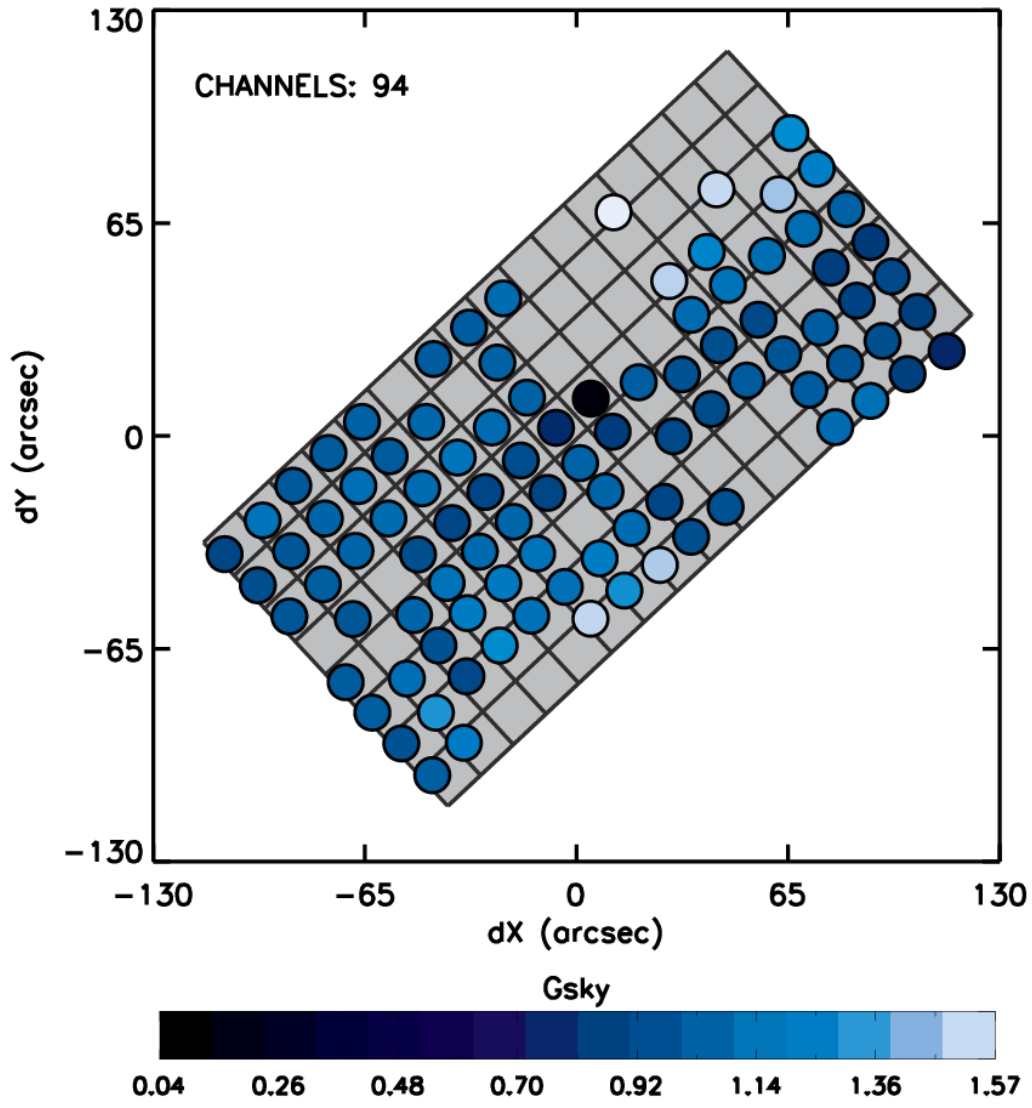

Figure 8: Pixel position in the field of view (filled circles) and sky gain (color code) obtained for one of the beam maps taken during the 3rd GISMO pool. The GISMO array (gray shaded grid) has been included for reference.

6 Data reduction

In the following we present the results obtained during the pool for the star forming region NGC 604 in M 33 . To reduce the data we used crush v 2.13-1.

The crush suite offers different filtering schemes:

- **default:** Standard pipeline reduction.
- **bright:** For bright point-like sources (e.g., planets and pointing sources).
- **faint:** For faint sources (S/N<30) but still visible in a single scan.
- **deep:** For very faint sources which are not at all detected in single scans. This setting results in the most aggressive filtering.
- **extended:** For structures larger than the field-of-view. This setting can be used alone or in combination with the above options.

We tested the filtering schemes *default*, *faint*, *deep*, and *extended*, as well as the combination *faint + extended*, which gave similar results to the extended filtering alone with the exception of a smoothing of half a beam.

NGC 604 is the second brightest star forming region of the Local Group after 30 Doradus. It is located in M 33. Optical studies reveal an age for this region of $\mathcal{T} = 4 \pm 1$ Myr (Hunter et al. 1996; González Delgado & Pérez 2000) and a total stellar mass of $M = (3.8 \pm 0.6) \times 10^5\,\mathrm{M}_\odot$ (Eldridge & Relaño 2011). The metallicity of NGC 604 has been measured to be about half-solar (Magrini et al. 2007).

NGC 604 (project 195-12) has been observed during the 3rd GISMO pool for a total of 3 hours. The observations consisted on $10' \times 10'$ on-the-fly maps at different rotation angles. A total of 45 scans were collected, all of them with a scan speed lower than $60\,''/s$. The median value of the NEFD was 17.80 mJy $\sqrt{\mathrm{s}}$. The scans were combined using crush. The filter schemes *default*, *faint*, *extended*, and *deep* were tested. The only acceptable results were obtained with *faint*. It was not possible to recover any extended emission.

The 2 mm flux of NGC 604, using the map generated with the *faint* filtering scheme and the aperture shown in Figure 9, was found to be 58 ± 4 mJy. In order to check the accuracy of this value, we compared the data from MIPS 24, 70, and 160 μm, SPIRE 250, 350, and 500 μm, GISMO 2 mm, and VLA 3.6 cm to the radiation transfer model of Groves et al. (2008) for a metallicity $Z = 0.4\,Z_\odot$ (no model with $Z = 0.5\,Z_\odot$ is available).

The best fit obtained is shown in Figure 10. The model fits the GISMO 2 mm data within the error bar, which was defined as the quadratic sum of the error due to background fluctuations (7%) and the calibration uncertainty (16%). The total stellar mass derived from the modeling is $M_{\mathrm{star}} = 3.89 \times 10^5\,\mathrm{M}_\odot$ and the age is $\mathcal{T} = 4.5$ Myr; both in agreement with the values found in the literature. The total dust luminosity is $L_{\mathrm{dust}} = 90 \times 10^6\,\mathrm{L}_\odot$. We want to stress that the modeling performed here does not pretend to be an exhaustive analysis of the SED of NGC 604 but a first approximation. A proper modeling, including aperture and color corrections, as well as line decontamination of the filters, is beyond the scope of this document.

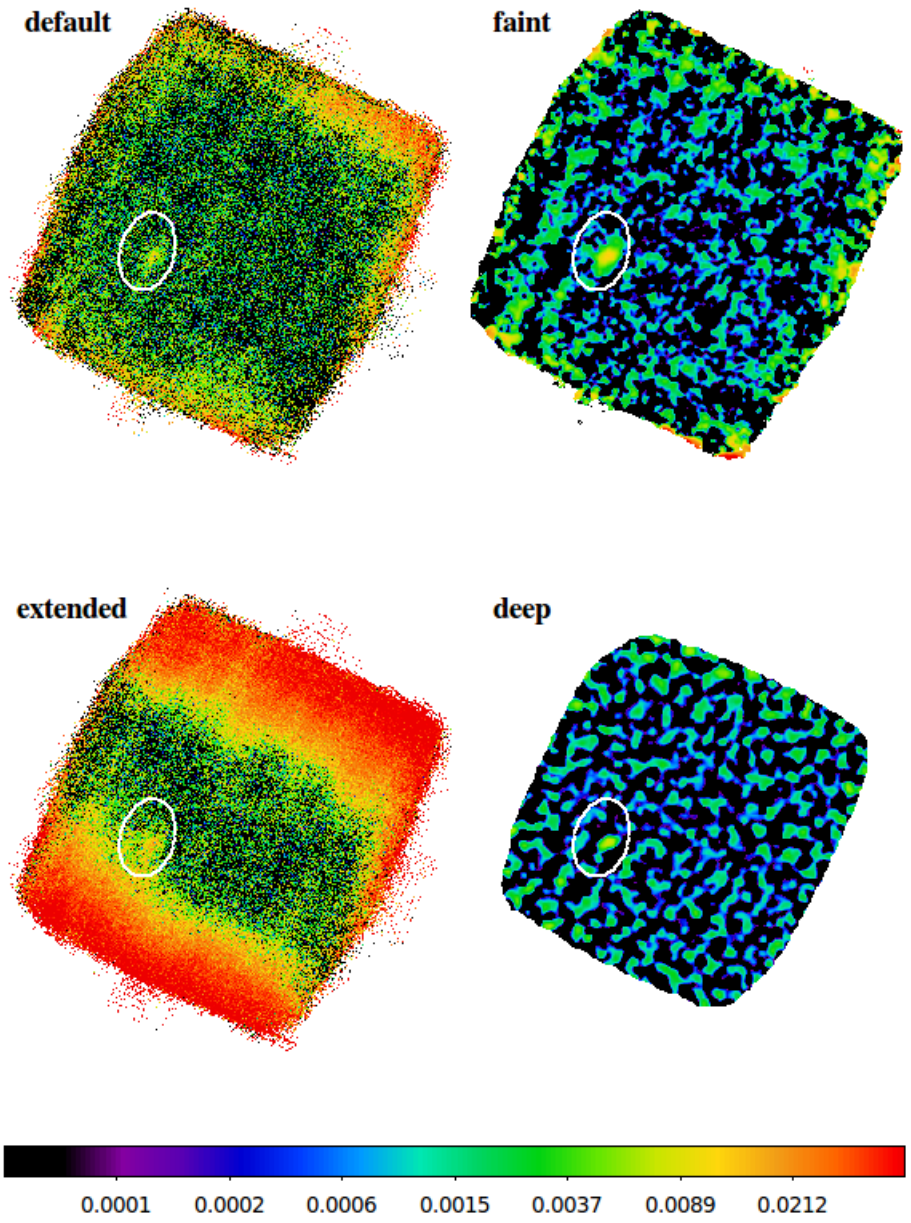

Figure 9: NGC 604 map reduced with different filter schemes. The elliptical aperture correspond to the aperture used to calculate the flux of NGC 604 and it is based on the flux distribution of the SPIRE 500 μm image.

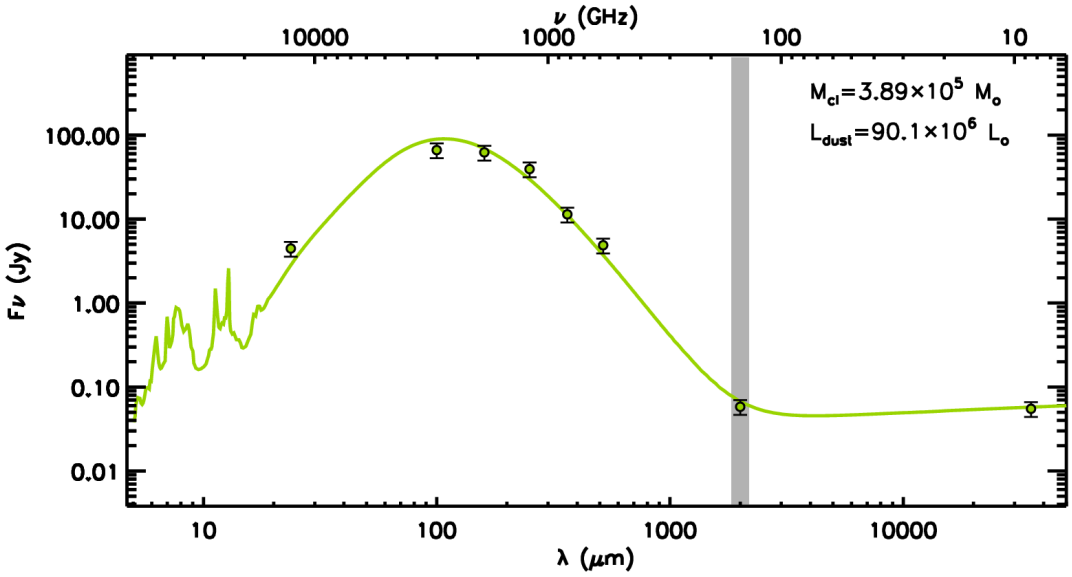

Figure 10: Best-fit model to the spectral energy distribution of the star forming region NGC 604. The value of the reduced χ^2 is 1.5.

References

Bruni, G. & Kramer, C. 2012

Bruni, G., Kramer, C., Billot, N., & Quintana-Lacaci, G. 2012

Eldridge, J. J. & Relaño, M. 2011, MNRAS, 411, 235

González Delgado, R. M. & Pérez, E. 2000, MNRAS, 317, 64

Groves, B., Dopita, M. A., Sutherland, R. S., et al. 2008, ApJS, 176, 438

Hunter, D. A., Baum, W. A., O'Neil, Jr., E. J., & Lynds, R. 1996, ApJ, 456, 174

Magrini, L., Vílchez, J. M., Mampaso, A., Corradi, R. L. M., & Leisy, P. 2007, A&A, 470, 865

Pardo, J. R., Cernicharo, J., & Serabyn, E. 2001, IEEE Transactions on Antennas and Propagation, 49, 1683

Sayers, J., Czakon, N. G., & Golwala, S. R. 2012, ApJ, 744, 169